

Merging black hole binaries: the effects of progenitor’s metallicity, mass-loss rate and Eddington factor

Nicola Giacobbo,^{1,2*} Michela Mapelli,^{2,3,4} Mario Spera,^{2,3,4}

¹*Dipartimento di Fisica e Astronomia “G. Galilei”, Università di Padova, vicolo dell’Osservatorio 3, I-35122*

²*INAF, Osservatorio Astronomico di Padova, vicolo dell’Osservatorio 5, I-35122 Padova, Italy.*

³*Institute for Astrophysics and Particle Physics, University of Innsbruck, Technikerstrasse 25/8, A-6020, Innsbruck, Austria*

⁴*INFN, Milano Bicocca, Piazza della Scienza 3, I-20126, Milano, Italy*

Accepted XXX. Received YYY; in original form ZZZ

ABSTRACT

The first four gravitational wave events detected by LIGO were all interpreted as merging black hole binaries (BHBs), opening a new perspective on the study of such systems. Here we use our new population-synthesis code MOBSE, an upgraded version of BSE (Hurley et al. 2002), to investigate the demography of merging BHBs. MOBSE includes metallicity-dependent prescriptions for mass loss of massive hot stars. It also accounts for the impact of the electron-scattering Eddington factor on mass loss. We perform $> 10^8$ simulations of isolated massive binaries, with 12 different metallicities, to study the impact of mass loss, core-collapse supernovae and common envelope on merging BHBs. Accounting for the dependence of stellar winds on the Eddington factor leads to the formation of black holes (BHs) with mass up to $65 M_{\odot}$ at metallicity $Z \sim 0.0002$. However, most BHs in merging BHBs have masses $\lesssim 40 M_{\odot}$. We find merging BHBs with mass ratios in the $0.1 - 1.0$ range, even if mass ratios > 0.6 are more likely. We predict that systems like GW150914, GW170814 and GW170104 can form only from progenitors with metallicity $Z \leq 0.006$, $Z \leq 0.008$ and $Z \leq 0.012$, respectively. Most merging BHBs have gone through a common envelope phase, but up to ~ 17 per cent merging BHBs at low metallicity did not undergo any common envelope phase. We find a much higher number of mergers from metal-poor progenitors than from metal-rich ones: the number of BHB mergers per unit mass is $\sim 10^{-4} M_{\odot}^{-1}$ at low metallicity ($Z = 0.0002 - 0.002$) and drops to $\sim 10^{-7} M_{\odot}^{-1}$ at high metallicity ($Z \sim 0.02$).

Key words: stars: black holes – black hole: physics – methods: numerical – gravitational waves – binaries: general – stars: mass-loss

1 INTRODUCTION

The first four direct detections of gravitational waves (GWs, Abbott et al. 2016a,b,c, 2017; The LIGO Scientific Collaboration et al. 2017) revolutionised our knowledge of black hole binaries (BHBs). Thanks to them, we now know that coalescing BHBs exist and can host massive black holes (BHs), with mass $\gtrsim 30 M_{\odot}$ (as in the case of GW150914, GW170104 and GW170814).

The formation and evolution of BHBs have been investigated for a long time (e.g. Tutukov et al. 1973; Thorne 1987; Schutz 1989; Kulkarni et al. 1993; Sigurdsson & Phinney 1993; Portegies Zwart & McMillan 2000; Colpi et al. 2003; Belczynski et al. 2004). Already before the first LIGO detection, several theoretical studies predicted the existence

of stellar BHs with mass $\gtrsim 30 M_{\odot}$ (e.g. Heger et al. 2003; Mapelli et al. 2009, 2010; Belczynski et al. 2010; Fryer et al. 2012; Mapelli et al. 2013; Spera et al. 2015). The basic idea is that if the pre-supernova mass of a star is sufficiently large (Fryer 1999; Fryer et al. 2001) and/or its pre-supernova compactness sufficiently high (O’Connor & Ott 2011), the star can collapse to a BH directly, producing a more massive remnant than in case of a supernova (SN) explosion.

Unfortunately, state-of-the-art theoretical models of BHBs still suffer from major uncertainties. The main issues are the treatment of core-collapse supernovae, stellar winds, and common envelope (CE, e.g. Dominik et al. 2012). The impact of stellar dynamics on the formation of BHBs is also matter of debate (e.g. Ziosi et al. 2014; Rodriguez et al. 2015, 2016; Mapelli 2016; Askar et al. 2016; Antonini et al. 2017; Banerjee 2017).

The physics of core-collapse SNe is remarkably complex

* E-mail: nicola.giacobbo@oapd.inaf.it

and barely understood (e.g. Fryer 1999; Heger & Woosley 2002; Heger et al. 2003; Fryer 2006; O'Connor & Ott 2011; Fryer et al. 2012; Janka 2012; Burrows 2013; Pejcha & Prieto 2015; Woosley 2017). The key point is to understand the connection between the final stages of a massive star's life and the outcome of a SN (for a review, see Limongi 2017). In particular, it is crucial to assess what are the conditions for a star to directly collapse into a BH, without an explosion (e.g. Bethe 1990; Fryer 1999; Fryer et al. 2001; Janka et al. 2007; O'Connor & Ott 2011; Janka 2012; Burrows 2013; Ertl et al. 2016).

Mass loss by stellar winds is also crucial, because it governs the final mass M_{fin} of a star, i.e. the mass of a star just before the SN (see e.g. Mapelli et al. 2009; Belczynski et al. 2010; Fryer et al. 2012; Mapelli et al. 2013). In the last decade, models of line-driven stellar winds were profoundly revised. Current models suggest a strong dependence of mass loss on metallicity ($\dot{M} \propto Z^\alpha$, with $\alpha \sim 0.85$, Vink et al. 2001, 2011; Muijres et al. 2012) not only during the main sequence (MS) but also after, including the Wolf-Rayet (WR) stage (see e.g. Vink & de Koter 2005; Meynet & Maeder 2005; Gräfener & Hamann 2008; Vink et al. 2011; Tang et al. 2014; Chen et al. 2015).

In addition, there has been a debate regarding the importance of stationary versus eruptive mass loss for massive star evolution (Vink & Gräfener 2012). Clumping of stellar winds results in a reduction of the mass-loss rate. Recent theoretical models (e.g. Vink et al. 2001) predict lower mass-loss rates by a factor of 2 – 3 with respect to unclumped empirical mass-loss rates, consistent with a moderate wind clumping.

Finally, some of the most recent wind models (e.g. Gräfener & Hamann 2008; Gräfener et al. 2011; Vink et al. 2011; Vink 2016) and observations (e.g. Bestenlehner et al. 2014) suggest that mass loss also depends on the electron-scattering Eddington factor Γ_e of the star. In particular, if a star approaches the Eddington limit (i.e. $\Gamma_e \lesssim 1$), stellar winds become almost insensitive to metallicity. Most stellar evolution models do not include this dependence, with very few exceptions (e.g. PARSEC, Chen et al. 2015). Population-synthesis codes, which are used to study the demography of BHs and BHBs, should also account for these updated models of stellar winds and massive star evolution.

Currently, only few population-synthesis codes adopt up-to-date metallicity-dependent prescriptions for stellar winds (e.g. Belczynski et al. 2010; Toonen et al. 2012; Mapelli et al. 2013; Spera et al. 2015; Spera & Mapelli 2017; Banerjee 2017). The dependence of stellar winds on the Eddington factor is implemented only in the SEVN code (where SEVN is the acronym for Stellar EVolution for N-body, Spera et al. 2015; Spera & Mapelli 2017). In its published version, SEVN only evolves single stars and is currently undergoing a major upgrade to include the main binary evolution processes (Spera et al., in preparation).

Here we present our upgraded version of BSE (acronym for Binary Stellar Evolution), one of the most popular population-synthesis codes (Hurley et al. 2000, 2002). In the following, we refer to our new version of BSE as MOBSE (which stands for 'Massive Objects in Binary Stellar Evolution'). With respect to BSE, MOBSE includes up-to-date equations for metal-dependent stellar winds (based on Belczynski et al. 2010 and on Chen et al. 2015) and new

prescriptions for core-collapse SNe (based on Fryer et al. 2012). Moreover, MOBSE includes the dependence of stellar winds on the Eddington factor, adopting the prescriptions by Chen et al. (2015).

We use MOBSE to investigate the formation of BHBs from isolated binaries, comparing different models of stellar winds and SNe. We also examine the role played by the CE phase in the formation of BHBs.

2 METHODS

In this Section, we describe the main features of MOBSE with respect to BSE.

2.1 Stellar winds and mass loss

MOBSE adopts the following prescriptions for stellar winds. For O and B stars with effective temperature $12500 \text{ K} \leq T \leq 25000 \text{ K}$ we adopt equation 25 of Vink et al. (2001):

$$\begin{aligned} \log \dot{M} = & -6.688 + 2.210 \log \left(\frac{L}{10^5 L_\odot} \right) \\ & -1.339 \log \left(\frac{M}{30 M_\odot} \right) - 1.601 \log \left(\frac{V}{2.0} \right) \\ & + \alpha \log \left(\frac{Z}{Z_\odot} \right) + 1.07 \log \left(\frac{T}{20000 \text{ K}} \right), \end{aligned} \quad (1)$$

where L is the stellar luminosity, M is the stellar mass, α expresses the dependence of mass loss on metallicity and $V = v_{\text{inf}}/v_{\text{esc}} = 1.3$ is the ratio of the wind velocity at infinity (v_{inf}) to escape velocity (v_{esc}).

For O and B stars with $25000 \text{ K} < T \leq 50000 \text{ K}$ we use equation 24 of Vink et al. (2001):

$$\begin{aligned} \log \dot{M} = & -6.697 + 2.194 \log \left(\frac{L}{10^5 L_\odot} \right) \\ & -1.313 \log \left(\frac{M}{30 M_\odot} \right) - 1.226 \log \left(\frac{V}{2.0} \right) \\ & + \alpha \log \left(\frac{Z}{Z_\odot} \right) + 0.933 \log \left(\frac{T}{40000 \text{ K}} \right) \\ & + 10.92 \left[\log \left(\frac{T}{40000 \text{ K}} \right) \right]^2, \end{aligned} \quad (2)$$

where $V = v_{\text{inf}}/v_{\text{esc}} = 2.6$. The above dichotomy is due to the bi-stability jump, i.e. a sudden jump in the mass-loss rate related to the fact that the iron ions driving the wind recombine at $T \sim 25000 \text{ K}$, and again below 12500 K (for more details see Vink et al. 1999; Petrov et al. 2016).

We express the mass loss of luminous blue variable (LBV) stars as

$$\dot{M} = 10^{-4} f_{\text{LBV}} \left(\frac{Z}{Z_\odot} \right)^\alpha M_\odot \text{ yr}^{-1}, \quad (3)$$

where f_{LBV} is a parameter (we choose $f_{\text{LBV}} = 1.5$, in agreement with Belczynski et al. 2010).

Finally, for Wolf-Rayet (WR) stars we use equation 9 of Belczynski et al. (2010):

$$\dot{M}_{\text{WR}} = 10^{-13} L^{1.5} \left(\frac{Z}{Z_\odot} \right)^\alpha M_\odot \text{ yr}^{-1}. \quad (4)$$

For the other stars, MOBSE adopts the same mass loss formalism as the original version of BSE.

2.1.1 MOBSE1

Equations 1, 2, 3 and 4, contain the parameter α which expresses the dependence of mass loss on metallicity. In our fiducial version of MOBSE (hereafter, MOBSE1), we define α in the following way:

$$\alpha = \begin{cases} 0.85 & \text{if } \Gamma_e < 2/3 \\ 2.45 - 2.4\Gamma_e & \text{if } 2/3 \leq \Gamma_e \leq 1, \end{cases} \quad (5)$$

where Γ_e is expressed as (see equation 8 of Gräfenor et al. 2011):

$$\log \Gamma_e = -4.813 + \log(1 + X_H) + \log(L/L_\odot) - \log(M/M_\odot), \quad (6)$$

where X_H is the Hydrogen fraction.

According to this definition, the dependence of mass loss on metallicity almost vanishes when the star is radiation pressure dominated ($\Gamma_e \sim 1$). This expression for α was derived by Tang et al. (2014) and Chen et al. (2015), based on the results of Gräfenor & Hamann (2008). In fact, Gräfenor & Hamann (2008) and Vink et al. (2011) show that the mass-loss rate is strongly enhanced when the star approaches the electron-scattering Eddington limit Γ_e . This means that increasing Γ_e the metallicity dependence becomes weaker.

2.1.2 MOBSE2

Other population-synthesis codes (e.g. STARTRACK, Belczynski et al. 2010) do not take into account the effect of Γ_e on mass loss. To quantify the importance of Γ_e and to compare our results with previous work, we also introduce a second version of our MOBSE code (which we will refer to as MOBSE2), where we do not include the effect of Γ_e .

In MOBSE2, the parameter α is defined as

$$\alpha = \begin{cases} 0.85 & \text{inequations 1 and 2} \\ 0 & \text{inequation 3} \\ 0.86 & \text{inequation 4.} \end{cases} \quad (7)$$

The values of α defined in equation 7 are the same as adopted by Belczynski et al. (2010). This implies that in MOBSE2 mass loss of O and B-type stars scales as $\dot{M} \propto Z^{0.85}$ (Vink et al. 2001). WR stars also show a similar dependence ($\alpha \sim 0.86$, Vink & de Koter 2005). Finally, the mass loss of LBVs does not depend on metallicity, as in equation 8 of Belczynski et al. (2010). This means that mass loss of LBVs is constant, while mass loss of MS and WR stars does not depend on Γ_e .

2.2 Supernovae

The physics of core-collapse SNe is uncertain and several different models exist (see Smartt 2009, for a review). For this reason, we have implemented two different prescriptions for core-collapse SNe (described in details by Fryer et al. 2012): i) the *rapid* SN model and ii) the *delayed* SN model.

The main difference between them is that they assume a different time-scale at which the explosion occurs: in the rapid (delayed) model the explosion takes place $t < 250$ ms ($t \gtrsim 0.5$ s) after core bounce.

Both the prescriptions depend only on the final mass of

the Carbon-Oxygen (CO) core (M_{CO}) and on the final mass of the star (M_{fin}), which determines the amount of fallback.

Other studies suggest a more complex relation between the properties of the star at the onset of collapse and the compact remnant mass (e.g. O'Connor & Ott 2011; Janka 2012; Ugliano et al. 2012; Pejcha & Prieto 2015; Ertl et al. 2016) and provide alternative formalisms to predict the remnant mass (e.g. the compactness criterion by O'Connor & Ott 2011 or the two-parameter criterion by Ertl et al. 2016). However, we cannot adopt these alternative formalisms in BSE, because they rely on the inner structure of the star at the onset of collapse, which is not calculated in BSE. Figure 21 of the recent review by Limongi (2017) shows that there is a strong correlation between the compactness parameter and the CO mass of the progenitor star, suggesting that our formalism based on the CO mass should give results similar to the formalism based on the compactness parameter in most cases (see also Figures 21 and 22 of Spera et al. 2015).

Furthermore, the rapid and delayed SN models do not distinguish between neutron stars (NSs) and BHs, because they are general prescriptions for the formation of compact remnants. According to the Tolman-Oppenheimer-Volkoff limit (Oppenheimer & Volkoff 1939), we assume that the minimum mass for a BH is $3.0M_\odot$ and all compact SN remnants with mass $< 3.0M_\odot$ are NSs.

The details of the implementation of core-collapse SNe in MOBSE can be found in Appendix A.

In MOBSE, we also added a formalism for pair-instability SNe (PISNe, Ober et al. 1983; Bond et al. 1984; Heger et al. 2003; Woosley et al. 2007) and pulsational pair-instability SNe (PPISNe, Barkat et al. 1967; Woosley et al. 2007; Chen et al. 2014; Yoshida et al. 2016), which are not included in BSE and in most population-synthesis codes. Our description of PISNe is based on the results by Heger et al. (2003): if the final Helium core mass ($M_{\text{He},f}$) of a star is $64M_\odot \lesssim M_{\text{He},f} \lesssim 135M_\odot$, we assume that the star leaves no remnant, because the ignition of Oxygen and Silicon releases enough energy to disrupt the entire star. If $M_{\text{He},f} > 135M_\odot$, the star is expected to avoid the PISN and to directly collapse into a BH.

Our description of PPISNe is based on the formalism presented in Spera et al. (2016) and Spera & Mapelli (2017) (see also Belczynski et al. 2016b; Woosley 2017). If the final mass of the Helium core is $32M_\odot \lesssim M_{\text{He},f} \lesssim 64M_\odot$, the star undergoes a PPISN and leaves a compact remnant whose mass is described by the fitting formulas in Appendix B.

We also updated the natal kick for BHs (V_{kick}) as follows (Fryer et al. 2012):

$$V_{\text{kick}} = (1 - f_{\text{fb}}) W_{\text{kick}}, \quad (8)$$

where f_{fb} is the fallback factor (the explicit expression can be found in Appendix A). W_{kick} is randomly drawn from a Maxwellian distribution with a one dimensional root-mean square $\sigma = 265 \text{ km s}^{-1}$. This distribution was derived by Hobbs et al. (2005), based on the proper motions of 233 isolated Galactic pulsars.

2.3 Additional changes in MOBSE

We also added to MOBSE the fitting formulas described in Hall & Tout (2014), to compute the core radius of evolved

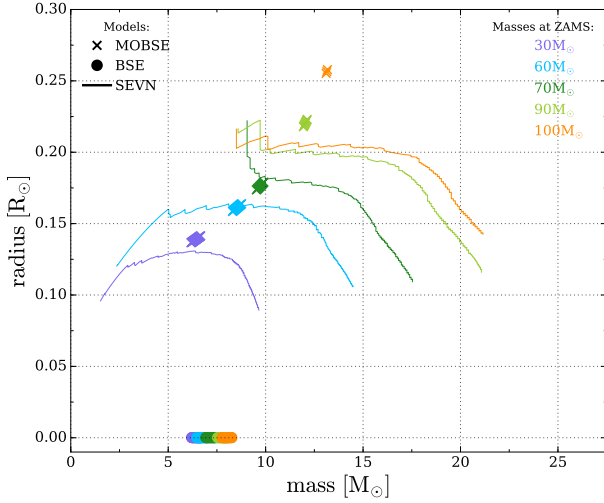


Figure 1. Radius versus mass of the CO core for five stars with zero-age main sequence (ZAMS) mass $M_{\text{ZAMS}} = 30, 60, 70, 90, 100 M_{\odot}$, at solar metallicity ($Z = 0.02$). Solid line: SEVN; crosses: MOBSE; circles: BSE.

stars. The core radius is crucial to determine the final fate of a CE system. Figure 1 shows the differences between the CO core radii computed with BSE (triangles), MOBSE (circles) and SEVN (lines) as a function of the core mass. The CO core radii derived with MOBSE are of the same order of magnitude as those obtained with SEVN, while BSE predicts unphysically small CO core radii. Our treatment of WR and LBV stars does not account for envelope inflation, which might increase the effective photospheric radii by a factor of ~ 10 (Gräfenr et al. 2012). We will include this effect in forthcoming studies.

Another critical issue of CE is the treatment of Hertzsprung Gap (HG) donors (e.g. de Mink & Belczynski 2015). During the HG phase, stars do not present a steep density gradient between the core and the envelope and for this reason their response to the CE phase should be similar to that of MS stars (see Ivanova & Taam 2004). In BSE, when a MS star enters a CE phase as donor it merges with the accretor, while HG donors are allowed to survive the CE phase. On the contrary, in MOBSE we imposed that even HG donors merge with their companions if they enter a CE phase (Dominik et al. 2012).

Finally, we also extended the mass range of BSE to include stars up to $150 M_{\odot}$. Because of the fitting formulas by Hurley et al. (2000) might be inaccurate for very massive stars ($> 100 M_{\odot}$) we imposed that the values of the stellar radii of single star are consistent with PARSEC stellar evolution tracks (Chen et al. 2015), as discussed in Mapelli (2016). We do not consider stars with zero-age main sequence (ZAMS) mass $M_{\text{ZAMS}} > 150 M_{\odot}$, because the mismatch between BSE fitting formulas and PARSEC tracks increases significantly above this mass (see e.g. Fig. 2).

Table 1. Initial conditions.

ID	Winds	SN	α	λ
MOBSE1_D	MOBSE1	delayed	1.0	0.1
MOBSE1_R	MOBSE1	rapid	1.0	0.1
MOBSE2_D	MOBSE2	delayed	1.0	0.1
MOBSE2_R	MOBSE2	rapid	1.0	0.1
MOBSE1_D1.5	MOBSE1	delayed	3.0	0.5
MOBSE1_D0.02	MOBSE1	delayed	0.2	0.1
MOBSE2_D1.5	MOBSE2	delayed	3.0	0.5
MOBSE2_D0.02	MOBSE2	delayed	0.2	0.1

Column 1: simulation name; column 2: stellar wind model (MOBSE1 and MOBSE2 see sec. 2.1); column 3: SN model (delayed and rapid from Fryer et al. 2012); column 4 and 5: values of α and λ in the CE formalism.

2.4 Simulations and initial distributions

In this section we detail the initial conditions of our population synthesis simulations. The mass of the primary star (m_1) is randomly extracted from a Kroupa initial mass function (Kroupa 2001),

$$\mathfrak{F}(m_1) \propto m_1^{-2.3} \quad \text{with } m_1 \in [5 - 150] M_{\odot}. \quad (9)$$

We sampled the mass of the secondary m_2 according to the distribution proposed by Sana et al. (2012)

$$\mathfrak{F}(q) \propto q^{-0.1} \quad \text{with } q = \frac{m_2}{m_1} \in [0.1 - 1] m_1, \quad (10)$$

We adopt the distributions proposed by Sana et al. (2012) also for the orbital period P and the eccentricity e :

$$\mathfrak{F}(\mathcal{P}) \propto (\mathcal{P})^{-0.55} \quad \text{with } \mathcal{P} = \log_{10}(P/\text{day}) \in [0.15 - 5.5] \quad (11)$$

and

$$\mathfrak{F}(e) \propto e^{-0.42} \quad \text{with } 0 \leq e < 1. \quad (12)$$

For the CE phase we adopted the same formalism used by Hurley et al. (2002) and described in detail in Ivanova et al. (2013). This formalism depends on two free parameters, α and λ , where, α is the fraction of orbital energy which can be used to unbind the envelope and λ describes the geometry of the envelope. In this work, we consider three different combinations of these parameters: $\alpha = 1.0$, $\lambda = 0.1$ (which is well motivated for massive stars, see e.g. Xu & Li 2010; Loveridge et al. 2011), $\alpha = 3.0$, $\lambda = 0.5$ and $\alpha = 0.2$, $\lambda = 0.1$.

We ran eight sets of simulations (see Table 1) in order to test different combinations of stellar wind models, SN explosion mechanisms and values of α and λ .

For each set of simulations we performed 12 sub-sets with different metallicities $Z = 0.0002, 0.0004, 0.0008, 0.0012, 0.0016, 0.002, 0.004, 0.006, 0.008, 0.012, 0.016$ and 0.02 . The polynomial fitting formulas implemented in BSE (Hurley et al. 2000) and the prescriptions for mass loss adopted in MOBSE have been shown to hold in this metallicity range (e.g. Kudritzki 2002; Bresolin & Kudritzki 2004). In each sub-set, we simulate 10^7 binary systems. Thus, each of the eight sets of simulations is composed of 1.2×10^8 massive binaries.

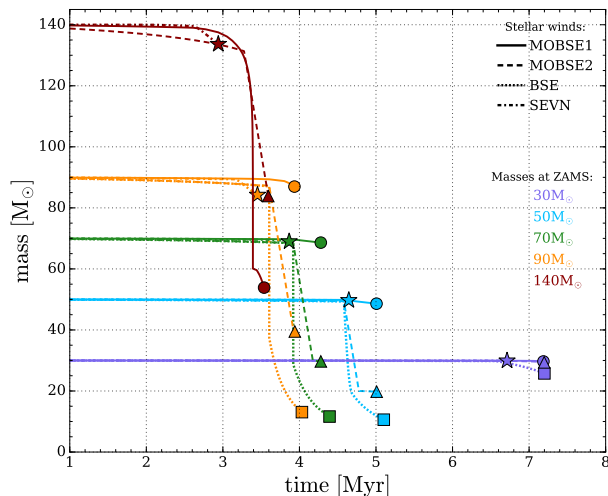


Figure 2. Stellar mass evolution with time for five different M_{ZAMS} at $Z = 0.0002$ computed with MOBSE, BSE and SEVN. Solid lines: MOBSE1; dashed lines: MOBSE2; dotted lines: BSE; dash-dot lines: SEVN. The markers identify the final mass of the stars: circles for MOBSE1, triangles for MOBSE2, squares for BSE and stars for SEVN.

3 RESULTS

3.1 Mass loss by stellar winds

In this Section, we discuss the evolution of single massive stars obtained with MOBSE1 and MOBSE2, in comparison to other open-source population synthesis codes, namely BSE (Hurley et al. 2000, 2002) and SEVN (Spera et al. 2015, 2016; Spera & Mapelli 2017). BSE is the original code from which MOBSE derives, while SEVN is a more recent code. In BSE single stellar evolution is implemented using polynomial fitting formulas (Hurley et al. 2000), while in SEVN stellar evolution is calculated from look-up tables (the current default tables are based on the recent PARSEC stellar evolution code, Bressan et al. 2012; Tang et al. 2014; Chen et al. 2015).

Figure 2 shows the evolution of stellar mass at $Z = 0.0002$ for various ZAMS masses. At low ZAMS masses ($\lesssim 30 M_{\odot}$) the behavior of the considered codes is quite indistinguishable. The main difference is the duration of stellar life in BSE and MOBSE with respect to the more updated SEVN code (see Fig. 2).

For larger ZAMS masses, there is a pronounced difference in the late evolutionary stages, due to the different stellar wind models. These differences are highlighted in Figure 3, which shows the final stellar mass (M_{fin}), as a function of the ZAMS mass (M_{ZAMS}) at $Z = 0.0002$. MOBSE1 is in remarkable agreement with SEVN for stars lighter than $M_{\text{ZAMS}} \simeq 100 M_{\odot}$, predicting a low mass loss during the entire star’s life. For more massive stars ($M_{\text{ZAMS}} > 100 M_{\odot}$), SEVN follows the same trend as for lighter stars, i.e. mass loss is extremely quenched, while the value of M_{fin} in model MOBSE1 drops to $\sim 50 M_{\odot}$.

The evolution of the stellar mass in MOBSE2 is generally intermediate between that of BSE and that of both

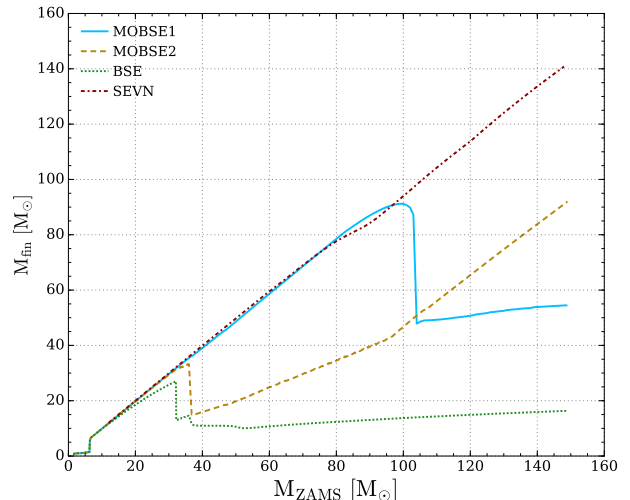


Figure 3. Final mass of a star (M_{fin}) as a function of its ZAMS mass at $Z = 0.0002$. Solid line: MOBSE1; dashed line: MOBSE2; dotted line: BSE; dash-dot line: SEVN. In all cases we considered the delayed SN model.

SEVN and MOBSE1. This difference arises mainly from the treatment of LBV stars. In both MOBSE1 and SEVN the mass loss scales as $\dot{M} \propto Z^{0.85}$, unless a star is radiation-pressure dominated ($\Gamma_e > 2/3$, see equations 5). In contrast, MOBSE2 assumes a strong mass loss rate for LBVs, independent of metallicity even if $\Gamma_e < 2/3$ (see equation 7).

3.2 Mass spectrum of compact remnants

Figure 4 shows the trend of the remnant mass (M_{rem}) as a function of M_{ZAMS} , for different values of the metallicity ($0.0002 \leq Z \leq 0.02$). In this Figure, we adopt the delayed mechanism for SN explosions. The upper and the lower panel show the results of MOBSE1 and MOBSE2, respectively. As expected, there is a relation between the maximum mass of the compact remnants and the metallicity: the lower the metallicity is, the higher the mass of the heaviest remnant.

At high metallicity ($Z = 0.02$) MOBSE1 and MOBSE2 are almost indistinguishable. In both models, the remnant mass increases monotonically with the ZAMS mass, until it reaches $M_{\text{rem}} \sim 20 M_{\odot}$.

At lower metallicities ($Z = 0.002$ and $Z = 0.0002$), MOBSE1 and MOBSE2 differ significantly, especially for $M_{\text{ZAMS}} > 30 M_{\odot}$. In MOBSE1 the remnant mass rapidly increases with M_{ZAMS} until it reaches its maximum ($M_{\text{rem}} \sim 50 - 65 M_{\odot}$) at $M_{\text{ZAMS}} \sim 70 M_{\odot}$. For larger ZAMS masses, the remnant mass drops to $\sim 40 M_{\odot}$. In MOBSE2 the remnant mass has a local maximum for $M_{\text{ZAMS}} \sim 30 M_{\odot}$. For larger ZAMS masses, it drops and then rises steadily to a global maximum of $M_{\text{rem}} \sim 40 M_{\odot}$ at $M_{\text{ZAMS}} > 120 M_{\odot}$.

Thus, the maximum BH mass predicted by MOBSE1 is $50 - 65 M_{\odot}$, significantly higher than the maximum BH mass predicted by MOBSE2 ($\sim 40 M_{\odot}$). The main reason for this difference is, again, the dependence of mass loss on the Eddington factor implemented in MOBSE1 but not in MOBSE2.

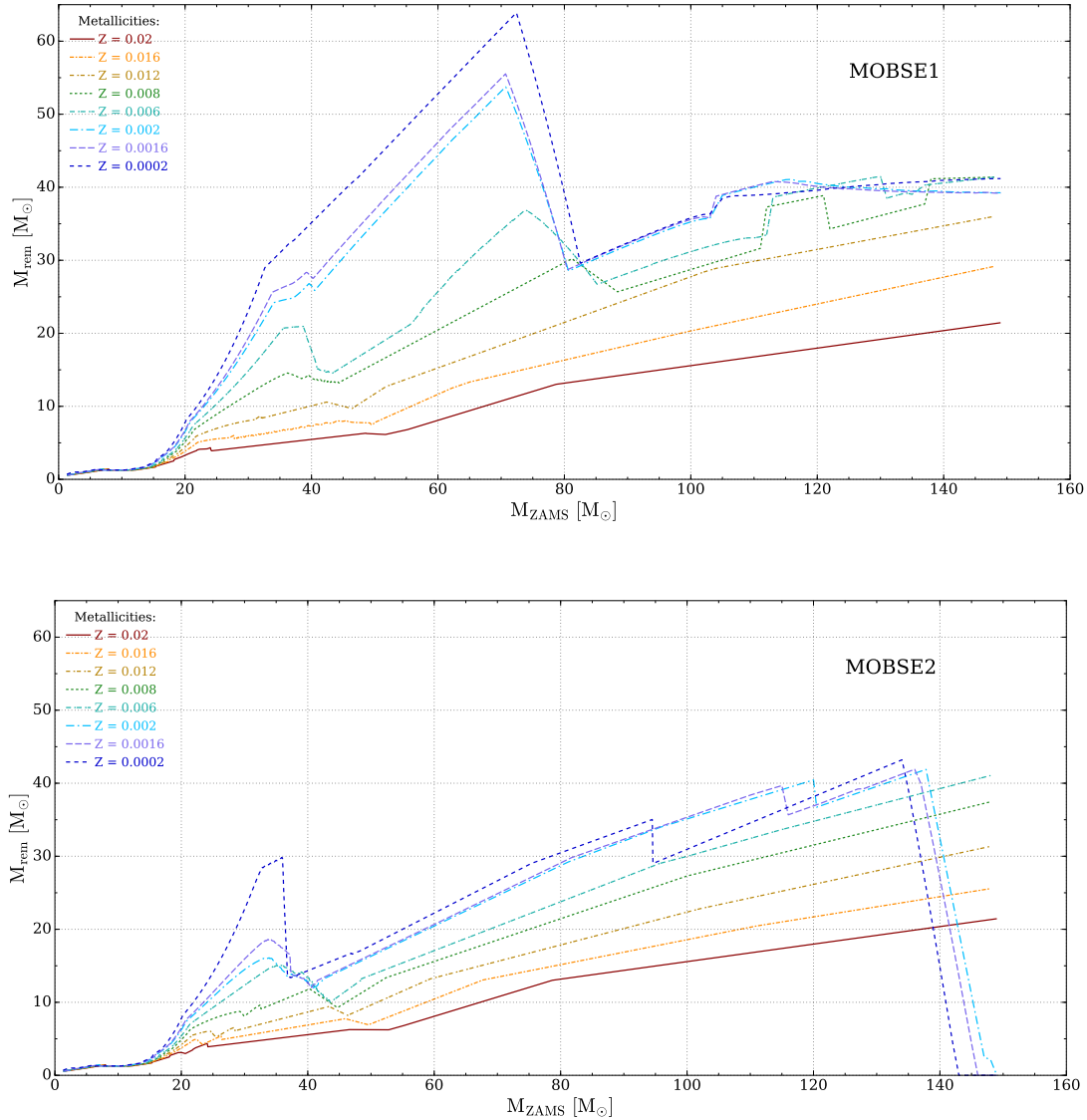


Figure 4. Mass of the compact remnant (M_{rem}) as a function of the ZAMS mass of the progenitor star, for different metallicities between $Z = 0.0002$ and 0.02 . Top: MOBSE1. Bottom: MOBSE2. In both cases we assume the delayed SN model.

Figure 5 compares the mass spectrum of compact remnants obtained with MOBSE, SEVN and BSE at three different metallicities. The dependence on metallicity is weaker for BSE, and stronger for both MOBSE and SEVN. At solar metallicity, all codes predict remnant masses $< 30 M_{\odot}$. At metallicity $Z = 0.002$ and $Z = 0.0002$, BSE is the only code predicting $M_{\text{rem}} < 30 M_{\odot}$, because of the stellar wind prescriptions. Both MOBSE and SEVN predict larger masses. We note that the BH mass spectrum obtained with MOBSE2 is in agreement with Belczynski et al. (2016a), who adopt similar prescriptions for the stellar winds (Belczynski et al. 2010).

At low metallicity ($Z < 0.002$) SEVN and MOBSE1 are in good agreement, while the remnant masses obtained with MOBSE2 are significantly different from both SEVN and MOBSE1. The key ingredient is again the fact that the stel-

lar wind prescriptions implemented in SEVN and MOBSE1 depend on both the metallicity and the Eddington factor.

The good agreement between SEVN and MOBSE1 is particularly remarkable, because SEVN (Spera & Mapelli 2017) adopts very recent stellar evolution models (from PARSEC, Bressan et al. 2012; Chen et al. 2015), while MOBSE1 is still based on the polynomial fitting formulas described by Hurley et al. (2000). This result confirms the importance of accounting for the Eddington factor in mass loss models.

In Figure 5 we can also note the effect of PISNe and PPISNe on the most massive metal-poor stars (see also Figure B1 in Appendix B). At metallicity $Z \leq 0.002$, very massive stars leave no remnant as an effect of PISNe in both MOBSE2 and SEVN. PISNe do not occur in MOBSE1 and BSE, because the final Helium core mass is always

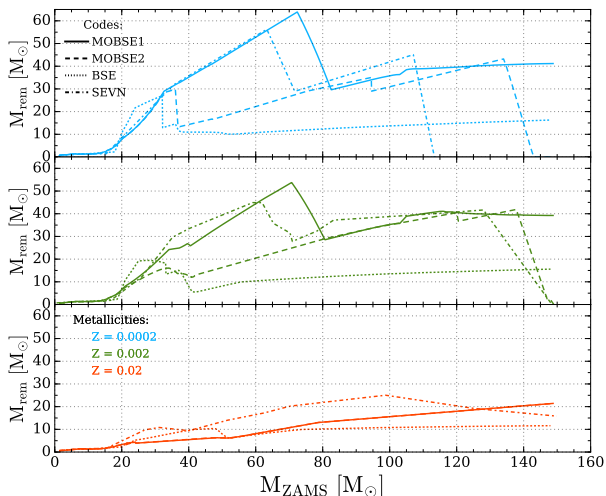


Figure 5. Mass of the compact remnant (M_{rem}) as a function of the ZAMS mass of the progenitor stars, for $Z = 0.02$ (bottom panel), $Z = 0.002$ (central panel) and $Z = 0.0002$ (top panel). Solid lines: MOBSE1; dashed lines: MOBSE2; dash-dot lines: SEVN; dotted lines: BSE. In all cases the delayed SN model is assumed.

below the threshold for PISNe ($\sim 64 M_{\odot}$). PPISNe occur in MOBSE1, MOBSE2 and SEVN at low metallicity ($Z \leq 0.008$ for MOBSE1 and SEVN and $Z \leq 0.002$ for MOBSE2) for stars with $32 M_{\odot} \lesssim M_{\text{He,f}} \lesssim 64 M_{\odot}$. Their effect is a substantial decrease of the remnant mass with respect to the final mass of the star (M_{fin} , Figure 3). PPISNe do not occur in BSE, because the final Helium core mass does not reach the threshold for PPISNe in BSE.

Figure 6 compares the rapid and the delayed core-collapse SN models. ZAMS masses larger than $50 M_{\odot}$ are not shown, because the rapid and the delayed SN models produce exactly the same remnant mass for $M_{\text{ZAMS}} > 50 M_{\odot}$, in agreement with Fryer et al. (2012) and Spera et al. (2015).

The main difference between rapid and delayed SN model is the number of remnants with mass $2 < M_{\text{rem}} < 5 M_{\odot}$. The rapid SN model predicts a mass gap between the lightest BHs ($\sim 5 M_{\odot}$) and the heaviest NSs ($\sim 2 M_{\odot}$), while the delayed model predicts no gap. This result is consistent with previous studies (Fryer et al. 2012; Spera et al. 2015). Dynamical mass measurements of compact objects in X-ray binaries show marginal indications for the existence of a mass gap (e.g. Özel et al. 2010; Farr et al. 2011), possibly suggesting a preference for a rapid SN explosion.

3.3 Black hole binaries (BHBs)

In this section, we focus on the properties of BHBs derived from our binary population-synthesis simulations with MOBSE. The left-hand panels of Figures 7 and 8 show the chirp mass¹ ($m_{\text{chirp}} = (m_p m_s)^{3/5} / (m_p + m_s)^{1/5}$, where m_p and

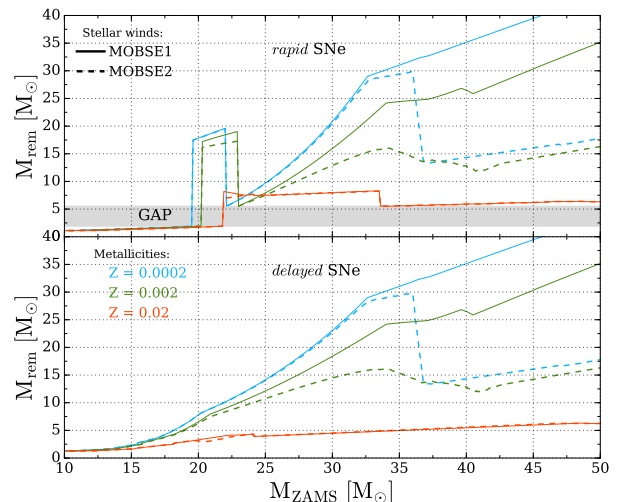


Figure 6. Mass of the compact remnant (M_{rem}) as a function of the ZAMS mass of the progenitor star (M_{ZAMS}) for two different core-collapse SN models: rapid SN model (upper panel) and delayed SN model (bottom panel). Red lines: metallicity $Z = 0.02$; green lines: $Z = 0.002$; blue lines: $Z = 0.0002$. Solid lines: MOBSE1, dashed lines: MOBSE2. In the top panel the mass gap between the heaviest NSs and the lightest BHs ($\sim 2 M_{\odot}$ to $\sim 5 M_{\odot}$) is highlighted by a shaded area.

m_s are the masses of the primary and secondary BH, respectively) and the total mass distributions of all BHBs which formed in our simulations MOBSE1.D and MOBSE2.D, including both BHBs which merge and BHBs which do not merge in a Hubble time. Simulations labelled as MOBSE1.D (MOBSE2.D) were run with MOBSE1 (MOBSE2), adopting the delayed SN model and assuming $\alpha = 1$, $\lambda = 0.1$ for the CE (see Table 1 for details on the simulations).

At low metallicity ($Z \lesssim 0.0004$), MOBSE1 produces very massive BHBs, with total mass up to $M_{\text{tot}} \simeq 150 M_{\odot}$ and chirp mass up to $M_{\text{chirp}} \simeq 55 M_{\odot}$, while the heaviest BHBs obtained with MOBSE2 have $M_{\text{tot}} \simeq 90 M_{\odot}$ and $M_{\text{chirp}} \simeq 40 M_{\odot}$. At solar metallicity ($Z = 0.02$), the maximum chirp mass (total mass) is $M_{\text{chirp}} \simeq 20 M_{\odot}$ ($M_{\text{tot}} \simeq 50 M_{\odot}$) for both MOBSE1 and MOBSE2.

We now restrict our attention to merging BHBs. The right-hand panels of Figures 7 and 8 show the chirp mass and the total mass distributions for the sub-sample of merging BHBs (defined as BHBs which merge within a Hubble time). It is apparent that the maximum mass of merging BHBs is significantly smaller than the maximum mass of non-merging BHBs. This difference persists at all metallicities, and is more pronounced in MOBSE1 than in MOBSE2.

The heaviest merging BHs have $M_{\text{BH,max}} \simeq 45 M_{\odot}$ (only few systems have a primary BH $\gtrsim 55 M_{\odot}$, in model MOBSE1) at $Z \leq 0.0002$ and $M_{\text{BH,max}} \simeq 20 M_{\odot}$ at $Z = 0.02$. The maximum values of the chirp masses are $M_{\text{chirp}} \simeq 40 M_{\odot}$ and $M_{\text{chirp}} \simeq 10 M_{\odot}$ at $Z = 0.0002$ and $Z = 0.02$, respectively.

¹ The chirp mass is named that because it is this combination of m_p and m_s that determines how fast the binary sweeps, or chirps, through a frequency band. In fact, it can be shown that the am-

plitude and the frequency of GWs scale as $m_{\text{chirp}}^{5/3}$ and $m_{\text{chirp}}^{-5/8}$, respectively (Maggiore 2008).

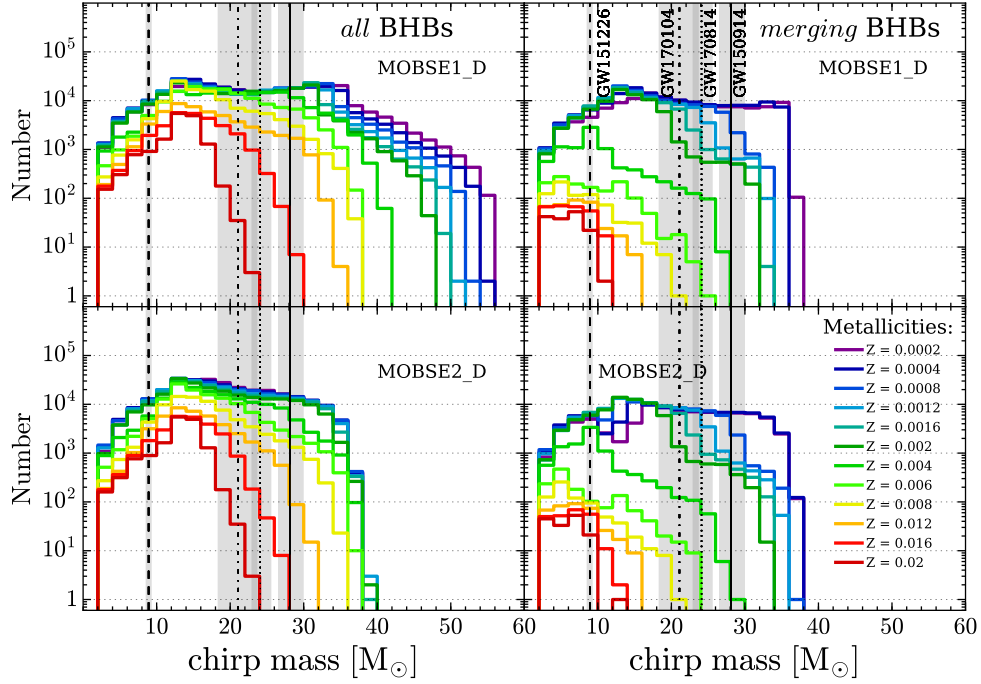


Figure 7. Chirp mass distribution of BHBs for MOBSE1.D (upper panels) and MOBSE2.D (lower panels). Left-hand column: chirp mass distribution for all BHBs. Right-hand column: chirp mass distribution for the merging BHBs only. Solid lines represent the chirp mass distributions at different metallicity, ranging from 0.0002 to 0.02. The vertical lines in all panels are the chirp masses of GW151226, GW150914 (Abbott et al. 2016a), GW170104 (Abbott et al. 2017) and GW170814 (The LIGO Scientific Collaboration et al. 2017) with the corresponding uncertainties (at the 90 per cent credible level, shadowed regions).

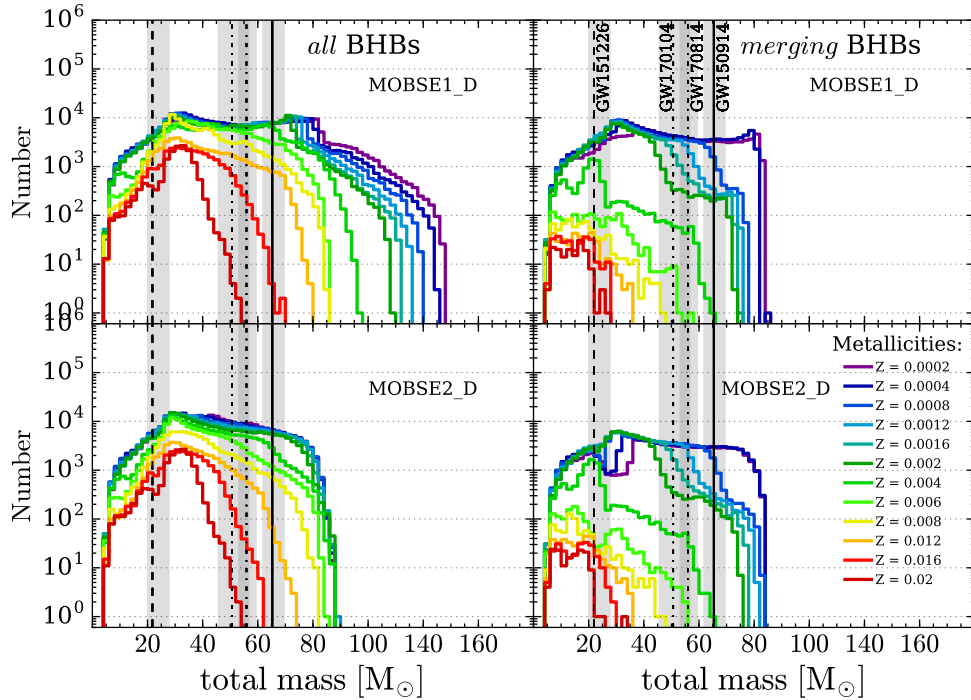


Figure 8. Same as Figure 7, but for the distribution of total masses.

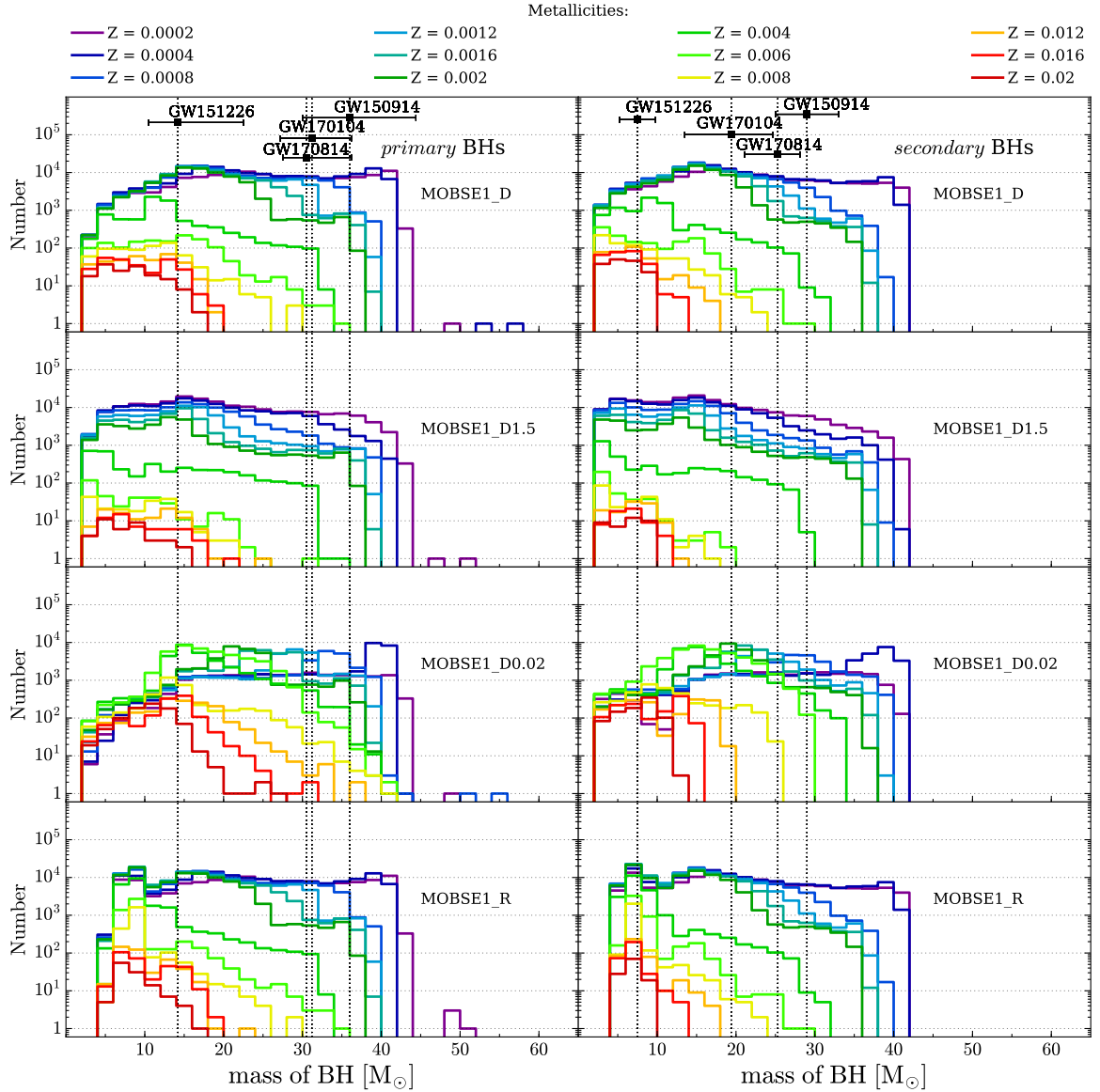


Figure 9. Mass distribution of primary (left-hand column) and secondary members (right-hand column) of merging BHBs in the eight simulation sets. Line colours (from red to violet) correspond to decreasing metallicity (from $Z = 0.02$ to $Z = 0.0002$). From top to bottom: MOBSE1_D, MOBSE1_D1.5, MOBSE1_D0.02, and MOBSE1_R. See Table 1 for details on each simulation. The vertical lines on the left-hand (right-hand) column are the mass of the primary (secondary) BH in GW151226, GW150914 (Abbott et al. 2016a), GW170104 (Abbott et al. 2017) and GW170814 (The LIGO Scientific Collaboration et al. 2017). The error bars show the uncertainties on each mass (at the 90 per cent credible level).

The masses of merging BHBs predicted by MOBSE1 are remarkably similar to those predicted by MOBSE2. This fundamental difference between merging BHBs and other BHBs holds for all eight sets of simulations performed in this paper, included those which are not shown in Figures 7 and 8. This happens because the most massive BHBs in MOBSE1 come from massive ($\sim 60 - 80 M_{\odot}$) progenitors which die as red super-giant stars. Thus, all such BHBs form with very large semi-major axis (otherwise their progenitors merge prematurely, due to their large radii) and cannot merge within a Hubble time.

Figures 7 to 8 also show that the number of BHBs scales inversely with the metallicity of the progenitors. This trend

is particularly strong if we consider only merging BHBs. This result originates from several factors. At higher metallicity, stars radii are larger, and thus a larger fraction of binaries merge before becoming a BHB. Moreover, we assume stronger SN kicks for lower BH masses. Thus, SN kicks are more efficient in unbinding light binaries, which are more common at high metallicity.

Figure 9 shows the distribution of masses of the primary BH (i.e. the most massive one) and of the secondary BH (i.e. the least massive one) for all merging BHBs in the four runs with MOBSE1. Figure 10 is the same for the four runs with MOBSE2. There are no significant differences between merging BHB masses in MOBSE1 and MOBSE2, regard-

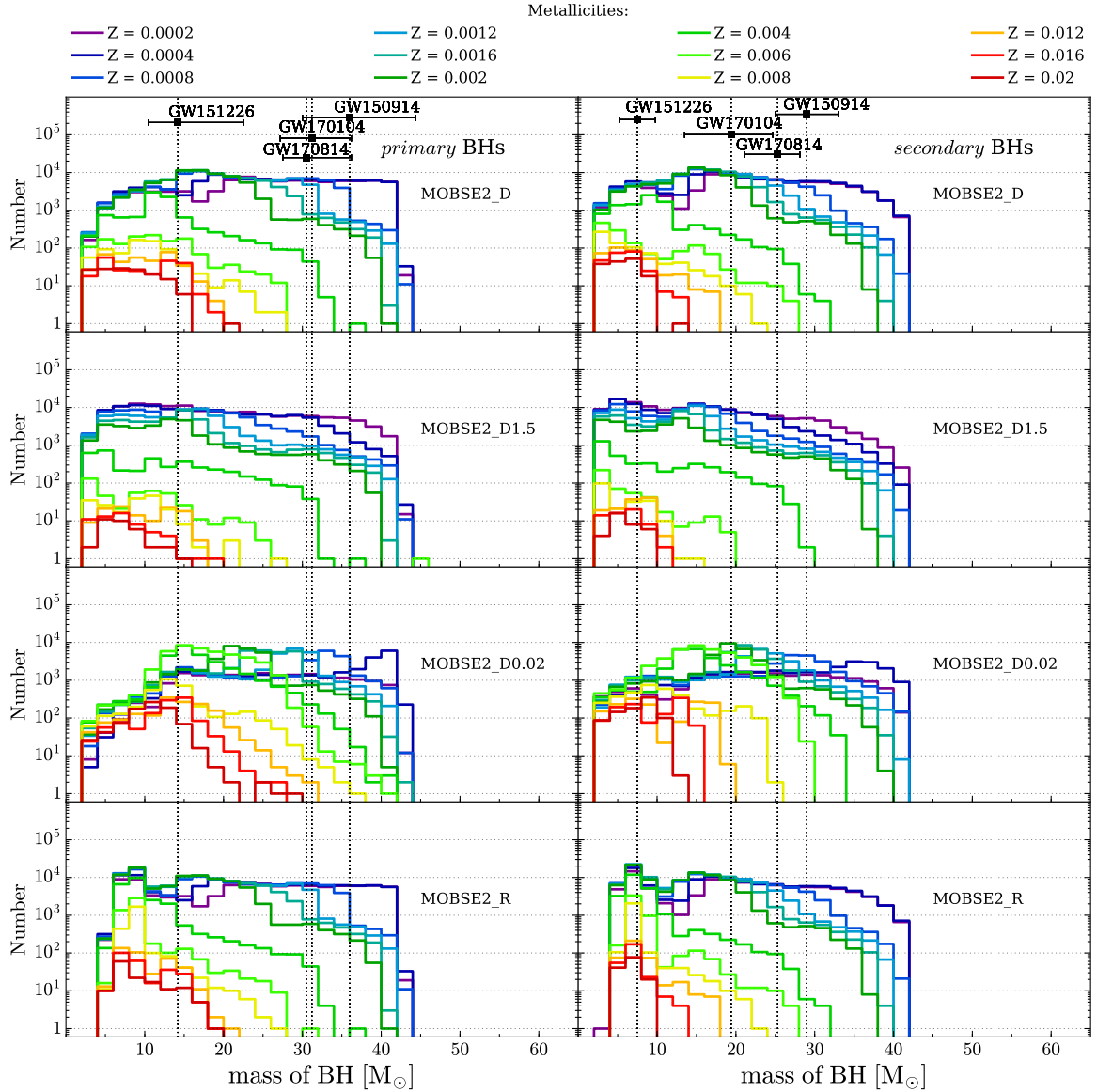


Figure 10. Same as Fig. 9 but for simulation with MOBSE2. From top to bottom: MOBSE2_D, MOBSE2_D1.5, MOBSE2_D0.02, and MOBSE2_R.

Table 2. Minimum metallicity of progenitors of GW events.

GW event	MOBSE1				MOBSE2			
	D1.5	D	D0.02	R	D1.5	D	D0.02	R
GW150914	$Z \leq 0.002$	$Z \leq 0.004$	$Z \leq 0.006$	$Z \leq 0.004$	$Z \leq 0.002$	$Z \leq 0.004$	$Z \leq 0.006$	$Z \leq 0.004$
LVT151012	$Z \leq 0.008$	$Z \leq 0.012$	$Z \leq 0.016$	$Z \leq 0.012$	$Z \leq 0.006$	$Z \leq 0.012$	$Z \leq 0.016$	$Z \leq 0.012$
GW151226	$Z \leq 0.02$	$Z \leq 0.02$	$Z \leq 0.02$	$Z \leq 0.02$	$Z \leq 0.02$	$Z \leq 0.02$	$Z \leq 0.02$	$Z \leq 0.02$
GW170104	$Z \leq 0.006$	$Z \leq 0.006$	$Z \leq 0.012$	$Z \leq 0.006$	$Z \leq 0.004$	$Z \leq 0.006$	$Z \leq 0.008$	$Z \leq 0.006$
GW170814	$Z \leq 0.004$	$Z \leq 0.006$	$Z \leq 0.008$	$Z \leq 0.006$	$Z \leq 0.004$	$Z \leq 0.004$	$Z \leq 0.008$	$Z \leq 0.004$

Column 1: GW detection; column 2-9: maximum star metallicity at which we can obtain merging BHBs with the same mass as the detected ones in runs MOBSE1_D1.5, MOBSE1_D, MOBSE1_D0.02, MOBSE1_R, MOBSE2_D1.5, MOBSE2_D, MOBSE2_D0.02, and MOBSE2_R (see Table 1).

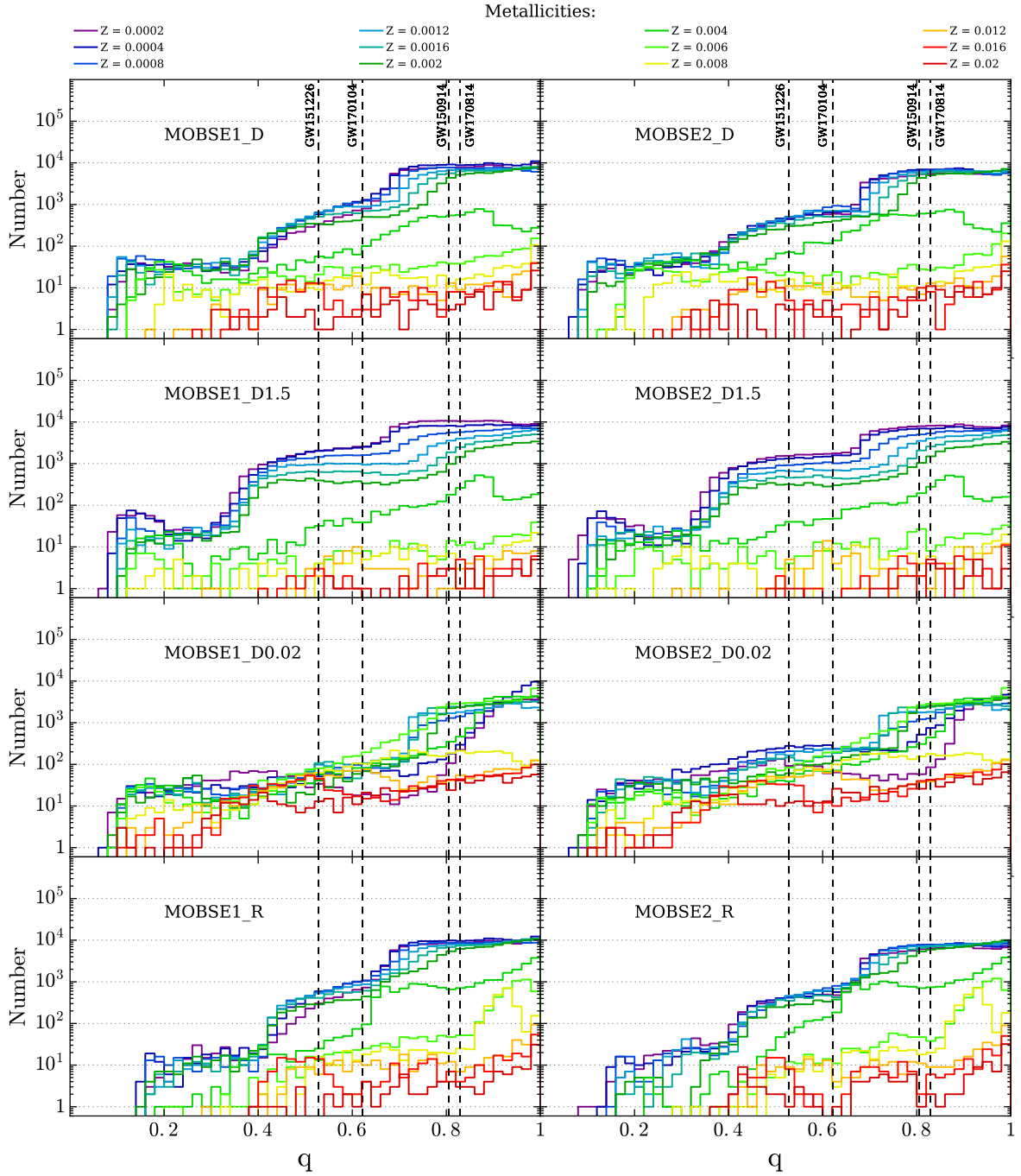


Figure 11. Distribution of the mass ratio $q = m_s/m_p$ (where m_p and m_s are the mass of the primary and of the secondary BH, respectively) of merging BHBs. Left-hand panel, from top to bottom: MOBSE1_D, MOBSE1_D1.5, MOBSE1_D0.02, MOBSE1_R. Right-hand panel, from top to bottom: MOBSE2_D, MOBSE2_D1.5, MOBSE2_D0.02, MOBSE2_R. The vertical lines are the mass ratio of GW151226, GW150914 (Abbott et al. 2016a), GW170104 (Abbott et al. 2017) and GW170814 (The LIGO Scientific Collaboration et al. 2017).

less of the SN model or CE prescription. The maximum mass of merging BHBs does not seem to depend significantly on the assumed SN model or on the assumed CE parameters. The minimum mass of merging BHBs does depend on the assumed SN model, because the rapid SN model (MOBSE1_R

and MOBSE2_R) does not allow to form compact remnants with mass in the range of $2 - 5 M_\odot$.

The main difference between different values of the CE parameters is the number of merging BHBs with relatively high metallicity ($0.006 \leq Z \leq 0.02$). The two models MOBSE1_D0.02 and MOBSE2_D0.02, which adopt $\alpha\lambda =$

0.02, form a significantly larger number of merging BHBs with relatively high metallicity ($0.006 \leq Z \leq 0.02$) than models with a larger value of $\alpha\lambda$. As already discussed in [Mapelli et al. \(2017\)](#), this is likely due to the fact that a lower value of $\alpha\lambda$ makes the spiral in of the cores much more efficient, bringing the two cores on a much smaller final orbital separation. Thus, even binaries with a very large initial orbital separation might give birth to a merging BHB system, provided that they can enter a CE phase. Entering a CE phase is much easier for metal-rich stars, because their radii are larger than those of their metal-poor analogues.

On the other hand, MOBSE1.D0.02 and MOBSE2.D0.02 also form a significantly smaller number of *light* merging BHBs ($< 12 M_\odot$) with relatively low metallicity ($Z < 0.006$) than models with a larger value of $\alpha\lambda$. This can be explained as follows. Assuming a lower value of $\alpha\lambda$ means that it is harder to eject the CE during the CE phase. This implies that the minimum semi-major axis (a_{\min}) above which a binary system survives the CE without merging is larger for a lower value of $\alpha\lambda$.

In the case of (both metal-rich and metal-poor) massive stars, the maximum stellar radii are always $\geq a_{\min}$ for the considered range of $\alpha\lambda$. This means that changes of $\alpha\lambda$ (and consequently of a_{\min}) do not affect the number of massive binary systems which merge prematurely (before becoming BHBs). In contrast, for light ($\lesssim 30 M_\odot$) metal-poor stars ($Z \leq 0.006$) this difference in a_{\min} is crucial, because the maximum stellar radii are $< a_{\min}$ for $\alpha\lambda = 0.02$ but $> a_{\min}$ for $\alpha\lambda \geq 0.1$. Therefore, the same binary will not survive the CE phase in the case with $\alpha\lambda = 0.02$, while it will survive without merging prematurely in the case with $\alpha\lambda \geq 0.1$. This effect explains the dearth of merging BHBs with $M < 12 M_\odot$ in MOBSE1.D0.02 and MOBSE2.D0.02 simulations respect to MOBSE1.D, MOBSE2.D, MOBSE1.D1.5 and MOBSE2.D1.5 simulations.

In addition, for metal-rich stars there is another effect that plays a role. Indeed, the spiral-in during CE is more efficient for small values of $\alpha\lambda$, so even initial larger binaries can become close binaries and eventually evolve into merging BHBs.

From Figures 9 and 10 and from Table 2 it is apparent that our models can account for all four GW events reported so far. The most massive systems (GW150914, GW170104 and GW170814) can be generated only by metal-poor progenitors. In particular, GW150914-like systems are produced only for $Z \leq 0.006$, GW170814-like systems for $Z \leq 0.008$, GW170104-like systems for $Z \leq 0.012$, and LVT151012-like systems for $Z \leq 0.016$, while GW151226-like systems exist at all metallicities ($Z \leq 0.02$, see Tab. 2 for details). From Tab. 2 it is also interesting to note that the higher $\alpha\lambda$ is, the lower the maximum metallicity to produce the observed GW events.

Finally, Figure 11 shows the mass ratio between the secondary BH and the primary BH in the merging BHBs. While nearly equal-mass systems are more common in our models, we find merging BHBs with nearly all possible mass ratios, down to $q \sim 0.1$. This is at odds with models of BHB formation through chemically homogeneous evolution ([Marchant et al. 2016](#); [de Mink & Mandel 2016](#); [Mandel & de Mink 2016](#)), which predict the formation of nearly equal mass merging BHBs, but is consistent with the mass ratio of the four GW detections.

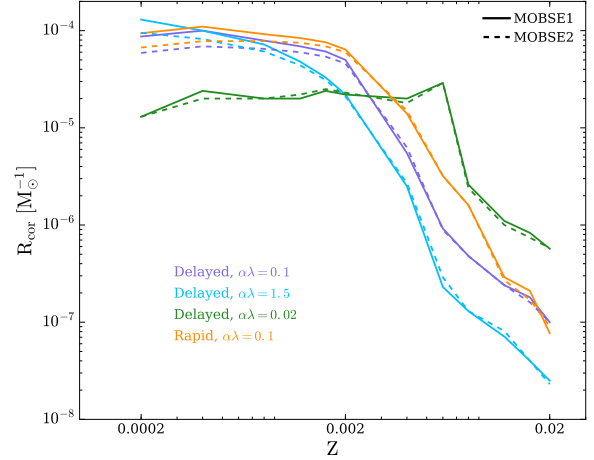


Figure 12. Corrected number of mergers per unit mass as a function of the metallicity for all sets of simulations. The colors identify different assumptions for the SN mechanism and for the values of CE parameters α and λ . Solid (dashed) lines: MOBSE1 (MOBSE2).

3.4 Mergers per unit mass

For each simulation, we calculate the number of merging BHBs per unit mass as

$$R = \frac{N_{\text{merger}}}{M_{\text{tot,sim}}}, \quad (13)$$

where N_{merger} is the number of merging BHBs in each sub-sample and $M_{\text{tot,sim}}$ is the total mass of the corresponding sub-sample.

This number must be corrected to account for the fact that we simulate only massive ($m_1 > 5 M_\odot$) binary systems (no single stars). We thus introduce the corrected number of merging BHBs per unit mass as

$$R_{\text{cor}} = f_{\text{bin}} f_{\text{IMF}} R, \quad (14)$$

where f_{bin} is the correction factor used to take into account that we only simulate binary systems. We put $f_{\text{bin}} = 0.5$, assuming that 50 per cent of stars are in binaries (see e.g. [Sana et al. 2013](#)). The correction factor $f_{\text{IMF}} = 0.285$ accounts for the fact that we actually simulate only systems with primary mass $m_1 \geq 5 M_\odot$. The values of R and R_{cor} are shown in Tables 3 and 4, respectively.

Figure 12 shows R_{cor} as a function of the metallicity Z for all simulations. R_{cor} strongly depends on the metallicity. In particular, R_{cor} is $\gtrsim 2$ orders of magnitude higher at low metallicity ($Z \lesssim 0.002$) than at high metallicity ($Z \sim 0.02$). This means that we form much more merging BHBs if the progenitors are metal-poor stars (see Tables 3 and 4).

3.5 Formation channels of merging BHBs

In Tables 5 and 6 we report the most common evolutionary pathways followed by merging BHBs in simulations MOBSE1 and MOBSE2, respectively. We distinguish three different formation channels: systems that **pass through a single CE phase (SCE)**; systems which experience multi-CE

Table 3. Merging BHBs in MOBSE1.

Z	MOBSE1_D1.5		MOBSE1_D		MOBSE1_D0.02		MOBSE1_R	
	N _{merger}	R _{cor} [M _⊙ ⁻¹]	N _{merger}	R _{cor} [M _⊙ ⁻¹]	N _{merger}	R _{cor} [M _⊙ ⁻¹]	N _{merger}	R _{cor} [M _⊙ ⁻¹]
0.0002	189837	1.3E-04	131819	8.7E-05	20259	1.3E-05	142137	9.4E-05
0.0004	157034	1.0E-04	152054	1.0E-04	35744	2.4E-05	164478	1.1E-04
0.0008	108094	7.2E-05	119200	7.9E-05	29503	2.0E-05	139294	9.2E-05
0.0012	73138	4.8E-05	104021	6.9E-05	30550	2.0E-05	126791	8.4E-05
0.0016	49989	3.3E-05	91747	6.1E-05	36228	2.4E-05	115196	7.6E-05
0.002	32747	2.2E-05	74888	5.0E-05	33812	2.2E-05	97099	6.4E-05
0.004	3766	2.5E-06	8356	5.5E-06	30511	2.0E-05	21602	1.4E-05
0.006	347	2.3E-07	1397	9.2E-07	43555	2.9E-05	4867	3.2E-06
0.008	203	1.3E-07	730	4.8E-07	3901	2.6E-06	2379	1.6E-06
0.012	107	7.1E-08	365	2.4E-07	1729	1.1E-06	438	2.9E-07
0.016	60	4.0E-08	276	1.8E-07	1260	8.3E-07	311	2.1E-07
0.02	38	2.5E-08	157	1.0E-07	867	5.7E-07	117	7.7E-08

Table 3. Column 1: metallicity; column 2-3: total number of merging BHBs and number of merging BHBs per unit mass at each metallicity for simulations MOBSE1_D1.5; column 4-5: same for MOBSE1_D; column 6-7: same for MOBSE1_D0.02; column 8-9: same for MOBSE1_R.

Table 4. Merging systems in MOBSE2.

Z	MOBSE2_D1.5		MOBSE2_D		MOBSE2_D0.02		MOBSE2_R	
	N _{merger}	R _{cor} [M _⊙ ⁻¹]	N _{merger}	R _{cor} [M _⊙ ⁻¹]	N _{merger}	R _{cor} [M _⊙ ⁻¹]	N _{merger}	R _{cor} [M _⊙ ⁻¹]
0.0002	142912	9.5E-05	89309	5.9E-05	19491	1.3E-05	100555	6.7E-05
0.0004	124392	8.2E-05	103508	6.9E-05	29680	2.0E-05	117595	7.8E-05
0.0008	92003	6.1E-05	97539	6.5E-05	30338	2.0E-05	118335	7.8E-05
0.0012	66391	4.4E-05	91225	6.0E-05	32842	2.2E-05	113580	7.5E-05
0.0016	46703	3.1E-05	81349	5.4E-05	37037	2.5E-05	104239	6.9E-05
0.002	31499	2.1E-05	68936	4.6E-05	34330	2.3E-05	90655	6.0E-05
0.004	4030	2.7E-06	9472	6.3E-06	27772	1.8E-05	22906	1.5E-05
0.006	438	2.9E-07	1351	8.9E-07	43231	2.9E-05	4821	3.2E-06
0.008	197	1.3E-07	722	4.8E-07	3598	2.4E-06	2414	1.6E-06
0.012	122	8.1E-08	369	2.4E-07	1567	1.0E-06	406	2.7E-07
0.016	60	4.0E-08	240	1.6E-07	1121	7.4E-07	259	1.7E-07
0.02	34	2.3E-08	153	1.0E-07	869	5.8E-07	138	9.1E-08

Same as Table 3 but for simulations MOBSE2_D1.5, MOBSE2_D, MOBSE2_D0.02 and MOBSE2_R.

phases (MCE); and systems that merge without CE phase (ZCE).

The vast majority of progenitors of merging BHBs undergo one CE phase ($> 80\%$), even if, especially at low metallicity ($Z < 0.004$), about 10–20 % of progenitors of merging BHBs do not experience any CE. Merging BHBs that went through multiple CE phases are a negligible fraction.

The percentage of ZCE systems increases with decreasing metallicity in both MOBSE1 and MOBSE2. The same trend was also noted by Dominik et al. (2012), but our results show a stronger dependence on the metallicity than Dominik et al. (2012).

4 CONCLUSIONS

We present the MOBSE code, our upgraded version of BSE. MOBSE includes up-to-date prescriptions for core-collapse SNe and for stellar winds. We account not only for the metallicity dependence of mass loss, but also for the effect of the Eddington factor (Vink et al. 2011; Chen et al. 2015; Vink

2016). We discuss two versions of MOBSE, MOBSE1 and MOBSE2. MOBSE2 implements the metallicity-dependent prescriptions described in Belczynski et al. (2010) and does not account for the effect of the Eddington factor, while MOBSE1 updates these prescriptions by accounting also for the Eddington factor (following Chen et al. 2015). Both versions of MOBSE also include recipes for PISNe and PPISNe, following Spera & Mapelli (2017).

The most massive BHs in MOBSE1 form at low metallicity ($Z \sim 0.0002 - 0.002$), reach a mass of $\sim 50 - 65 M_{\odot}$ and come from progenitor stars with ZAMS mass $M_{\text{ZAMS}} \sim 60 - 80 M_{\odot}$. In contrast, the most massive BHs in MOBSE2 form at low metallicity ($Z \sim 0.0002 - 0.002$), but reach a lower mass of $\sim 40 M_{\odot}$ and come from progenitor stars with ZAMS mass $M_{\text{ZAMS}} \gtrsim 120 M_{\odot}$ (Figure 4).

The distribution of BH masses derived with MOBSE2 is in good agreement with the one discussed by Belczynski et al. (2010, 2016a), who adopt similar prescriptions for stellar winds and SNe. The distribution of BH masses obtained with MOBSE1 is significantly different from that produced by MOBSE2 and is remarkably similar to the one derived

with the SEVN code (Spera & Mapelli 2017). This is not surprising, because both MOBSE1 and SEVN account for the impact of the Eddington factor on mass loss, but is quite remarkable, because stellar evolution in MOBSE is still based on the polynomial fitting formulas described in Hurley et al. (2000), while SEVN adopts the recent PARSEC stellar evolution models (Bressan et al. 2012; Chen et al. 2015). This result also indicates that the Eddington factor has a large impact on the distribution of BH masses.

We have studied the demography of BHBs, performing a large set of population-synthesis simulations with both MOBSE1 and MOBSE2. We perform simulations with different models of core-collapse SN (delayed versus rapid models, Fryer et al. 2012) and changing the efficiency of CE.

The distribution of simulated BHB masses covers the entire mass spectrum of BHs predicted by MOBSE1 and MOBSE2 from single stellar evolution (Fig. 4). However, if we consider only merging BHBs (defined as BHBs which are expected to merge in a Hubble time), their maximum mass is significantly lower. Even at the lowest metallicity, the maximum mass of merging BHBs is $\sim 55 M_{\odot}$ and $\sim 45 M_{\odot}$ in MOBSE1 and in MOBSE2, respectively. This indicates that the most massive BHBs in MOBSE1 do not merge. The most likely explanation is that these BHBs come from massive ($\sim 60 - 80 M_{\odot}$) progenitors which die as red supergiant stars. Thus, all such BHBs form with very large semi-major axis (otherwise their progenitors merge prematurely, due to their large radii) and do not merge in a Hubble time. This feature is nearly independent of the CE parameters and of the SN model.

The maximum mass of merging BHs formed in our simulations ($\approx 45 M_{\odot}$) is consistent with the possible upper mass gap suggested by LIGO-Virgo detections (i.e. the dearth of merging BHs with mass in the $\sim 50 - 135 M_{\odot}$ range, Fishbach & Holz 2017).

We find merging BHBs with mass ratios in the $0.1 - 1.0$ range, even if mass ratios > 0.6 are more likely. The masses of our merging BHBs match those of the four observed GW events. In our MOBSE1 and MOBSE2 simulations, systems like GW150914, LVT151012, GW151226, GW170104 and GW170814 could have formed only from binaries with metallicity $Z \leq 0.006$, ≤ 0.016 , ≤ 0.02 , ≤ 0.012 and ≤ 0.008 , respectively.

The vast majority of progenitors of merging BHBs undergo one CE phase ($> 80\%$), even if, especially at low metallicity ($Z < 0.004$), about $10 - 20\%$ of progenitors of merging BHBs do not experience any CE. Merging BHBs that went through multiple CE phases are a negligible fraction.

Merging BHBs form much more efficiently from metal-poor than from metal-rich binaries, both in MOBSE1 and in MOBSE2. The number of BHB mergers per unit mass is $\sim 10^{-4} M_{\odot}^{-1}$ at low metallicity ($Z = 0.0002 - 0.002$) and drops to $\sim 10^{-7} M_{\odot}^{-1}$ at high metallicity ($Z \sim 0.02$, Fig. 12). This trend of the number of BHB mergers per unit mass with the progenitor's metallicity potentially has a crucial impact on GW observations across cosmic time.

ACKNOWLEDGEMENTS

We thank the anonymous referee for their comments which significantly improved this paper. We thank Alessandro

Table 5. Formation channels of BHBs in MOBSE1.D.

Z	N° of mergers	Channels	Fraction
0.02	157	ZCE	0%
		SCE	100%
		MCE	0%
0.016	276	ZCE	0.36%
		SCE	98.19%
		MCE	1.45%
0.012	365	ZCE	0.27%
		SCE	95.89%
		MCE	3.84%
0.008	730	ZCE	0.41%
		SCE	95.21%
		MCE	4.38%
0.006	1397	ZCE	1.00%
		SCE	95.71%
		MCE	3.29%
0.004	8356	ZCE	17.52%
		SCE	81.08%
		MCE	1.40%
0.002	74888	ZCE	8.42%
		SCE	91.01%
		MCE	0.57%
0.0016	91747	ZCE	7.94%
		SCE	91.34%
		MCE	0.72%
0.0012	104021	ZCE	8.13%
		SCE	90.73%
		MCE	1.14%
0.0008	119200	ZCE	8.97%
		SCE	89.43%
		MCE	1.60%
0.0004	152054	ZCE	9.16%
		SCE	89.99%
		MCE	0.86%
0.0002	131819	ZCE	12.68%
		SCE	86.35%
		MCE	0.97%

Column 1: metallicity; column 2: total number of BHBs that merge within an Hubble time; column 3: formation channels, considering systems that evolve with zero CE phase (ZCE), with single CE phase (SCE) and with multiple CE phases (MCE); column 4: percentage of the merging BHBs which evolve through a given channel.

Bressan for useful discussions. We acknowledge the "Accordo Quadro INAF-CINECA (2017)" for the availability of high performance computing resources and support. MM and MS acknowledge financial support from the Italian Ministry of Education, University and Research (MIUR) through grant FIRB 2012 RBFR12PM1F, and from INAF through grant PRIN-2014-14. MM acknowledges financial support from the MERAC Foundation.

REFERENCES

- Abbott B. P., et al., 2016a, *Physical Review X*, **6**, 041015
 Abbott B. P., et al., 2016b, *Physical Review Letters*, **116**, 061102
 Abbott B. P., et al., 2016c, *ApJ*, **818**, L22

Table 6. Formation channels of BHBs in MOBSE2.D.

Z	N° of mergers	Channels	Fraction
0.02	153	ZCE	0.65%
		SCE	96.73%
		MCE	2.61%
0.016	240	ZCE	0.00%
		SCE	96.67%
		MCE	3.33%
0.012	369	ZCE	0.27%
		SCE	96.75%
		MCE	2.98%
0.008	722	ZCE	0.83%
		SCE	94.32%
		MCE	4.85%
0.006	1351	ZCE	2.74%
		SCE	92.23%
		MCE	5.03%
0.004	9472	ZCE	16.69%
		SCE	82.19%
		MCE	1.12%
0.002	68936	ZCE	9.66%
		SCE	89.91%
		MCE	0.43%
0.0016	81349	ZCE	9.62%
		SCE	89.90%
		MCE	0.48%
0.0012	91225	ZCE	10.14%
		SCE	88.61%
		MCE	1.25%
0.0008	9705	ZCE	11.71%
		SCE	86.37%
		MCE	1.93%
0.0004	103508	ZCE	13.71%
		SCE	85.07%
		MCE	1.22%
0.0002	89309	ZCE	17.46%
		SCE	81.13%
		MCE	1.41%

Same as Table 5 but for MOBSE2.

Abbott B. P., et al., 2017, *Physical Review Letters*, **118**, 221101
Antonini F., Toonen S., Hamers A. S., 2017, *ApJ*, **841**, 77
Askar A., Giersz M., Pych W., Olech A., Hypki A., 2016, in Meiron Y., Li S., Liu F.-K., Spurzem R., eds, IAU Symposium Vol. 312, Star Clusters and Black Holes in Galaxies across Cosmic Time. pp 262–263 ([arXiv:1501.00417](#)), [doi:10.1017/S1743921315007991](#)
Banerjee S., 2017, preprint, ([arXiv:1707.00922](#))
Barkat Z., Rakavy G., Sack N., 1967, *Physical Review Letters*, **18**, 379
Belczynski K., Sadowski A., Rasio F. A., 2004, *ApJ*, **611**, 1068
Belczynski K., Bulik T., Fryer C. L., Ruiter A., Valsecchi F., Vink J. S., Hurley J. R., 2010, *ApJ*, **714**, 1217
Belczynski K., Holz D. E., Bulik T., O’Shaughnessy R., 2016a, *Nature*, **534**, 512
Belczynski K., et al., 2016b, *A&A*, **594**, A97
Bestenlehner J. M., et al., 2014, *A&A*, **570**, A38
Bethe H. A., 1990, *Reviews of Modern Physics*, **62**, 801
Bond J. R., Arnett W. D., Carr B. J., 1984, *ApJ*, **280**, 825
Bresolin F., Kudritzki R. P., 2004, Origin and Evolution of the Elements, p. 283

Bressan A., Marigo P., Girardi L., Salasnich B., Dal Cero C., Rubele S., Nanni A., 2012, *MNRAS*, **427**, 127
Burrows A., 2013, *Reviews of Modern Physics*, **85**, 245
Chen K.-J., Woosley S., Heger A., Almgren A., Whalen D. J., 2014, *ApJ*, **792**, 28
Chen Y., Bressan A., Girardi L., Marigo P., Kong X., Lanza A., 2015, *MNRAS*, **452**, 1068
Colpi M., Mapelli M., Possenti A., 2003, *ApJ*, **599**, 1260
Dominik M., Belczynski K., Fryer C., Holz D. E., Berti E., Bulik T., Mandel I., O’Shaughnessy R., 2012, *ApJ*, **759**, 52
Ertl T., Janka H.-T., Woosley S. E., Sukhbold T., Ugliano M., 2016, *ApJ*, **818**, 124
Farr W. M., Sravan N., Cantrell A., Kreidberg L., Bailyn C. D., Mandel I., Kalogera V., 2011, *ApJ*, **741**, 103
Fishbach M., Holz D. E., 2017, preprint, ([arXiv:1709.08584](#))
Fryer C. L., 1999, *ApJ*, **522**, 413
Fryer C. L., 2006, *New Astron. Rev.*, **50**, 492
Fryer C. L., Woosley S. E., Heger A., 2001, *ApJ*, **550**, 372
Fryer C. L., Belczynski K., Wiktorowicz G., Dominik M., Kalogera V., Holz D. E., 2012, *ApJ*, **749**, 91
Gräfenor G., Hamann W.-R., 2008, *A&A*, **482**, 945
Gräfenor G., Vink J. S., de Koter A., Langer N., 2011, *A&A*, **535**, A56
Gräfenor G., Owocki S. P., Vink J. S., 2012, *A&A*, **538**, A40
Hall P. D., Tout C. A., 2014, *MNRAS*, **444**, 3209
Heger A., Woosley S. E., 2002, *ApJ*, **567**, 532
Heger A., Fryer C. L., Woosley S. E., Langer N., Hartmann D. H., 2003, *ApJ*, **591**, 288
Hobbs G., Lorimer D. R., Lyne A. G., Kramer M., 2005, *MNRAS*, **360**, 974
Hurley J. R., Pols O. R., Tout C. A., 2000, *MNRAS*, **315**, 543
Hurley J. R., Tout C. A., Pols O. R., 2002, *MNRAS*, **329**, 8 97
Ivanova N., Taam R. E., 2004, *ApJ*, **601**, 1058
Ivanova N., et al., 2013, *A&ARv*, **21**, 59
Janka H.-T., 2012, *Annual Review of Nuclear and Particle Science*, **62**, 407
Janka H.-T., Langanke K., Marek A., Martínez-Pinedo G., Müller B., 2007, *Phys. Rep.*, **442**, 38
Kroupa P., 2001, *MNRAS*, **322**, 231
Kudritzki R. P., 2002, *ApJ*, **577**, 389
Kulkarni S. R., Hut P., McMillan S., 1993, *Nature*, **364**, 421
Limongi M., 2017, preprint, ([arXiv:1706.01913](#))
Loveridge A. J., van der Sluys M. V., Kalogera V., 2011, *ApJ*, **743**, 49
Maggiore M., 2008, *Classical and Quantum Gravity*, **25**, 209002
Mandel I., de Mink S. E., 2016, *MNRAS*, **458**, 2634
Mapelli M., 2016, *MNRAS*, **459**, 3432
Mapelli M., Colpi M., Zampieri L., 2009, *MNRAS*, **395**, L71
Mapelli M., Ripamonti E., Zampieri L., Colpi M., Bressan A., 2010, *MNRAS*, **408**, 234
Mapelli M., Zampieri L., Ripamonti E., Bressan A., 2013, *MNRAS*, **429**, 2298
Mapelli M., Giacobbo N., Ripamonti E., Spera M., 2017, preprint, ([arXiv:1708.05722](#))
Marchant P., Langer N., Podsiadlowski P., Tauris T. M., Moriya T. J., 2016, *A&A*, **588**, A50
Meynet G., Maeder A., 2005, *A&A*, **429**, 581
Muijres L. E., Vink J. S., de Koter A., Müller P. E., Langer N., 2012, *A&A*, **537**, A37
O’Connor E., Ott C. D., 2011, *ApJ*, **730**, 70
Ober W. W., El Eid M. F., Fricke K. J., 1983, *A&A*, **119**, 61
Oppenheimer J. R., Volkoff G. M., 1939, *Physical Review*, **55**, 374
Özel F., Psaltis D., Narayan R., McClintock J. E., 2010, *ApJ*, **725**, 1918
Pejcha O., Prieto J. L., 2015, *ApJ*, **806**, 225
Petrov B., Vink J. S., Gräfenor G., 2016, *MNRAS*, **458**, 1999
Portegies Zwart S. F., McMillan S. L. W., 2000, *ApJ*, **528**, L17

- Rodriguez C. L., Morscher M., Pattabiraman B., Chatterjee S., Haster C.-J., Rasio F. A., 2015, *Physical Review Letters*, **115**, 051101
- Rodriguez C. L., Zevin M., Pankow C., Kalogera V., Rasio F. A., 2016, *ApJ*, **832**, L2
- Sana H., et al., 2012, *Science*, **337**, 444
- Sana H., et al., 2013, *A&A*, **550**, A107
- Schutz B. F., 1989, in Hellings R. W., ed., NASA Conference Publication Vol. 3046, NASA Conference Publication.
- Sigurdsson S., Phinney E. S., 1993, *ApJ*, **415**, 631
- Smartt S. J., 2009, *Annual Review of Astronomy & Astrophysics*, **47**, 63
- Spera M., Mapelli M., 2017, *MNRAS*, **470**, 4739
- Spera M., Mapelli M., Bressan A., 2015, *MNRAS*, **451**, 4086
- Spera M., Giacobbo N., Mapelli M., 2016, preprint, ([arXiv:1606.03349](https://arxiv.org/abs/1606.03349))
- Tang J., Bressan A., Rosenfield P., Slemmer A., Marigo P., Girardi L., Bianchi L., 2014, *MNRAS*, **445**, 4287
- The LIGO Scientific Collaboration et al., 2017, preprint, ([arXiv:1709.09660](https://arxiv.org/abs/1709.09660))
- Thorne K. S., 1987, *Science*, **236**, 1007
- Timmes F. X., Woosley S. E., Weaver T. A., 1996, *ApJ*, **457**, 834
- Toonen S., Nelemans G., Portegies Zwart S., 2012, *A&A*, **546**, A70
- Tutukov A., Yungelson L., Klayman A., 1973, *Nauchnye Informatsii*, **27**, 3
- Ugliano M., Janka H.-T., Marek A., Arcones A., 2012, *ApJ*, **757**, 69
- Vink J. S., 2016, preprint, ([arXiv:1610.00578](https://arxiv.org/abs/1610.00578))
- Vink J. S., Gräfener G., 2012, *ApJ*, **751**, L34
- Vink J. S., de Koter A., 2005, *A&A*, **442**, 587
- Vink J. S., de Koter A., Lamers H. J. G. L. M., 1999, *A&A*, **350**, 181
- Vink J. S., de Koter A., Lamers H. J. G. L. M., 2001, *A & A*, **369**, 574
- Vink J. S., Muijres L. E., Anthonisse B., de Koter A., Gräfener G., Langer N., 2011, *A&A*, **531**, A132
- Woosley S. E., 2017, preprint, ([arXiv:1608.08939](https://arxiv.org/abs/1608.08939))
- Woosley S. E., Blinnikov S., Heger A., 2007, *Nature*, **450**, 390
- Xu X.-J., Li X.-D., 2010, *ApJ*, **716**, 114
- Yoshida T., Takahashi K., Umeda H., Ishidoshiro K., 2016, *Phys. Rev. D*, **93**, 123012
- Ziosi B. M., Mapelli M., Branchesi M., Tormen G., 2014, *MNRAS*, **441**, 3703
- de Mink S. E., Belczynski K., 2015, *ApJ*, **814**, 58
- de Mink S. E., Mandel I., 2016, *MNRAS*, **460**, 3545

APPENDIX A: CORE-COLLAPSE SNE

In the following we summarize the main features of the rapid and delayed core-collapse SN mechanisms proposed by Fryer et al. (2012).

In both cases, compact objects form from a proto-compact object M_{pro} that accretes mass from the fallback material M_{fb} which can follow the SN explosion,

$$M_{\text{fb}} = f_{\text{fb}}(M_{\text{fin}} - M_{\text{pro}}), \quad (\text{A1})$$

where M_{fin} is the final mass of the star and f_{fb} is the fallback factor. Starting from the baryonic mass of the compact object, $M_{\text{rem,bar}} = M_{\text{pro}} + M_{\text{fb}}$, and considering the mass loss due to neutrinos it is possible to compute the gravitational mass $M_{\text{rem,grav}}$. We use the formula suggested by Timmes et al. (1996) for the NSs

$$M_{\text{rem,grav}} = \frac{\sqrt{1 + 0.3M_{\text{rem,bar}} - 1}}{0.15}, \quad (\text{A2})$$

and the same approach described in Fryer et al. (2012) for BHs,

$$M_{\text{rem,grav}} = 0.9M_{\text{rem,bar}}. \quad (\text{A3})$$

A0.1 Rapid

For the rapid mechanisms, it is assumed a fixed mass of the proto-object, $M_{\text{pro}} = 1.0 M_{\odot}$. The value of the fallback factor depends on the mass of the CO core M_{CO} and is given by

$$f_{\text{fb}} = \begin{cases} \frac{0.2}{M_{\text{fin}} - M_{\text{pro}}} & \text{if } M_{\text{CO}}/M_{\odot} < 2.5 \\ \frac{0.286M_{\text{CO}} - 0.514 M_{\odot}}{M_{\text{fin}} - M_{\text{pro}}} & \text{if } 2.5 \leq M_{\text{CO}}/M_{\odot} < 6.0 \\ 1.0 & \text{if } 6.0 \leq M_{\text{CO}}/M_{\odot} < 7.0 \\ \alpha_{\text{R}}M_{\text{CO}} + \beta_{\text{R}} & \text{if } 7.0 \leq M_{\text{CO}}/M_{\odot} < 11.0 \\ 1.0 & \text{if } 11.0 \leq M_{\text{CO}}/M_{\odot}, \end{cases} \quad (\text{A4})$$

where

$$\alpha_{\text{R}} \equiv 0.25 - \frac{1.275}{M_{\text{fin}} - M_{\text{pro}}} \quad \beta_{\text{R}} \equiv 1 - 11\alpha_{\text{R}}. \quad (\text{A5})$$

The direct collapse of a star into a BH occurs when $f_{\text{fb}} = 1.0$ and for the rapid model it is verified in two intervals of core masses, $6.0 M_{\odot} \leq M_{\text{CO}} < 7.0 M_{\odot}$ and $11.0 M_{\odot} \leq M_{\text{CO}}$

A0.2 Delayed

For the delayed model, even the mass of the proto-compact object depends on M_{CO} and it is given by,

$$M_{\text{pro}} = \begin{cases} 1.2 M_{\odot} & \text{if } M_{\text{core}}/M_{\odot} < 2.5 \\ 1.3 M_{\odot} & \text{if } 3.5 \leq M_{\text{CO}}/M_{\odot} < 6.0 \\ 1.4 M_{\odot} & \text{if } 6.0 \leq M_{\text{CO}}/M_{\odot} < 11.0 \\ 1.6 M_{\odot} & \text{if } 11.0 \leq M_{\text{CO}}/M_{\odot}. \end{cases} \quad (\text{A6})$$

The fallback factor is computed by using the following expressions

$$f_{\text{fb}} = \begin{cases} \frac{0.2}{M_{\text{fin}} - M_{\text{pro}}} & \text{if } M_{\text{CO}}/M_{\odot} < 2.5 \\ \frac{0.5M_{\text{CO}} - 1.05 M_{\odot}}{M_{\text{fin}} - M_{\text{pro}}} & \text{if } 2.5 \leq M_{\text{CO}}/M_{\odot} < 3.5 \\ \alpha_{\text{D}}M_{\text{CO}} + \beta_{\text{D}} & \text{if } 3.5 \leq M_{\text{CO}}/M_{\odot} < 11.0 \\ 1.0 & \text{if } 11.0 \leq M_{\text{CO}}/M_{\odot}, \end{cases} \quad (\text{A7})$$

where

$$\alpha_{\text{D}} \equiv 0.133 - \frac{0.093}{M_{\text{fin}} - M_{\text{pro}}} \quad \beta_{\text{D}} \equiv 1 - 11\alpha_{\text{D}}. \quad (\text{A8})$$

Thus, for the delayed model the direct collapse of a star into a BH occurs only if $11.0 M_{\odot} \leq M_{\text{CO}}$.

APPENDIX B: PISNE & PPISNE

In the following we detail the formulas implemented in MOBSE to describe PPISNe and PISNe, following the prescriptions described in Spera et al. (2016) and Spera & Mapelli (2017).

To compute the mass of the compact remnant we adopted the formula

$$M_{\text{rem}} = f_{\text{p}}M_{\text{rem,nop}}, \quad (\text{B1})$$

where $M_{\text{rem,nop}}$ is the mass of the compact remnant we would

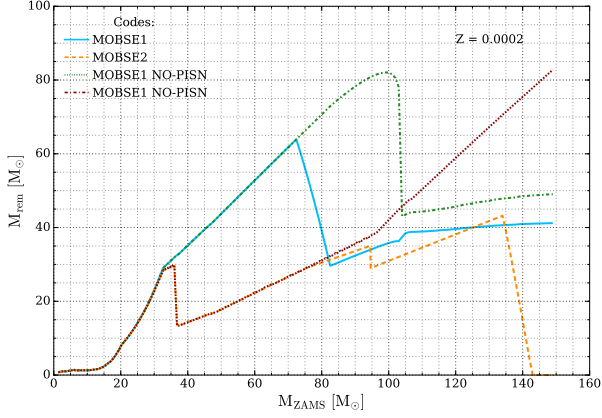


Figure B1. Effect of the PISNe and PPISNe on the mass spectrum of the remnants as a function of the M_{ZAMS} at $Z = 0.0002$. Solid-blue line: MOBSE1 with PISNe and PPISNe; dash-dot-green line: MOBSE1 without PISNe and PPISNe; dashed-yellow line: MOBSE2 with PISNe and PPISNe; dotted-red line: MOBSE2 without PISNe and PPISNe.

obtain without PPISNe and PISNe and f_p is a factor depending on the final Helium core mass of the star. In particular, $f_p = 1$ means that remnants will form via direct collapse and $f_p = 0$ means that remnants will completely destroy due to PISNe. In Fig. B1 we show the mass spectrum with/without PPISNe and PISNe for both MOBSE1 and MOBSE2 at $Z = 0.0002$.

We use the following expressions to compute f_p distinguishing between H-rich stars and WR stars.

B0.2 WR stars

$$f_p = \begin{cases} 1.0 & \text{if } M_{\text{He}}/M_{\odot} \leq 32 \\ (M_{\text{He}} - 32.0)(0.5226 \frac{M_{\text{He}}}{M_{\text{tot}}} - 0.52974) + 1.0 & \text{if } 32 < M_{\text{He}}/M_{\odot} \leq 37 \\ (-0.1381 \frac{M_{\text{He}}}{M_{\text{tot}}} + 0.1309)(M_{\text{He}} - 56) + 0.82916 & \text{if } 37 < M_{\text{He}}/M_{\odot} \leq 56 \\ -0.103645 M_{\text{He}} + 6.63328 & \text{if } 56 < M_{\text{He}}/M_{\odot} < 64 \\ 0.0 & \text{if } 64 \leq M_{\text{He}}/M_{\odot} < 135 \\ 1.0 & \text{if } 135 \leq M_{\text{He}}/M_{\odot}. \end{cases} \quad (\text{B4})$$

This paper has been typeset from a \LaTeX file prepared by the author.

B0.1 Normal stars

$$f_p = \begin{cases} 1.0 & \text{if } M_{\text{He}}/M_{\odot} \leq 32 \\ \frac{(k-1.0)}{5.0} M_{\text{He}} + \frac{(37.0-32.0\alpha_n)}{5.0} & \text{if } 32 < M_{\text{He}}/M_{\odot} \leq 37 \\ \alpha_n & \text{if } 37 < M_{\text{He}}/M_{\odot} \leq 60 \\ -\frac{\alpha_n}{4.0} M_{\text{He}} + 16.0\alpha_n & \text{if } 60 < M_{\text{He}}/M_{\odot} < 64 \\ 0.0 & \text{if } 64 \leq M_{\text{He}}/M_{\odot} < 135 \\ 1.0 & \text{if } 135 \leq M_{\text{He}}/M_{\odot}, \end{cases} \quad (\text{B2})$$

where α_n is given by

$$\alpha_n = 0.67 \frac{M_{\text{He}}}{M_{\text{tot}}} + 0.1. \quad (\text{B3})$$